# Electron-phonon coupling and mobility modeling in organic semiconductors: method and application to tetracene polymorphs

Patrizio Graziosi<sup>1,\*</sup>, Raffaele Guido Della Valle<sup>2</sup>, Tommaso Salzillo<sup>2</sup>, Simone d'Agostino<sup>3</sup>, Martina Zangari, Elisabetta Cané<sup>2</sup>, Matteo Masino<sup>4</sup>, Elisabetta Venuti<sup>2,\*</sup>

- <sup>1</sup> ISMN CNR, Consiglio Nazionale delle Ricerche, via Gobetti 101, 40129, Bologna, Italy
- <sup>2</sup> Dipartimento di Chimica Industriale "Toso Montanari", Università di Bologna, via Gobetti 85, 410129, Italy
- <sup>3</sup> Dipartimento di Chimica "Giacomo Ciamician", Università di Bologna, Via F. Selmi, 2, 40126 Bologna, Italy
- <sup>4</sup> Dipartimento di Scienze Chimiche, Della Vita e Della Sostenibilità Ambientale & INSTM-UdR Parma, Parco Area delle Scienze, 17/A, 43124 Parma, Italy
- \* patrizio.graziosi@cnr.it, elisabetta.venuti@unibo.it

#### **Abstract**

We have developed a first-principles method to calculate the electron-phonon coupling for specific modes and **q**-points in the Brillouin Zone for crystalline organic semiconductors. Using the obtained coupling strengths, we propose an approach to compute the temperature-dependent mobilities of electrons and holes. This methodology is applied to both bulk and thin-film polymorphs of tetracene. To validate our treatment of the electronic structures and vibrational properties, we calculate the Raman spectra in the lattice-phonon region and compare them with experimental data. We then compare the computed mobilities with available data for single crystals, finding good agreement within the experimental range, especially when accounting for possible charged impurities. Finally, we discuss the observed differences between the polymorphs.

## I. Introduction

Organic Semiconductors (OSCs) with proper functionalization have emerged as attractive candidates as active layers in several new electronic technologies. These encompass various applications from displays (OLED) to unconventional flexible, stretchable and/or wearable devices, phototransistors, easy processable large area electronics, organic photovoltaics (OPV), energy storage (redox flow batteries, organic electrodes, pseudo-/super-capacitors, gas storage and separation), photocatalytic systems, sensing applications, and others. [1–4] Moreover, OSCs are based on abundant, eco-friendly, and cheap elements, nominally C, O, N, S, with negligible content of critical raw materials. This hallmark is crucial in the development of the next generation of sustainable functional materials.

However, the widespread application of OSCs in electronics-related applications is hampered by the lack of predictive understanding of the inter-relationship between solid-state packing and performance of the device (whatever type of device). This challenge also arises from the existence of multiple crystal structures, known as polymorphism, for a given molecular compound. Each polymorph exhibits a distinct vibrational pattern, leading to variations in electron-phonon coupling (EPC), thereby influencing the transport characteristics of OSCs. [4–6] Indeed, low-frequency vibrational modes, such as translations and rotations of the entire molecule, play a pivotal role in introducing dynamic disorder. This dynamic disorder, in turn, affects on-site energies and electronic transfer integrals, ultimately shaping the macroscale electronic properties of the semiconductor. Therefore, understanding polymorphism is crucial for defining the electronic properties in OSCs at a macroscopic scale.

On the predictive modelling ground, charge transport models are worth a mention. Although sophisticated and computationally intensive approaches exist (such as mean field models, open quantum systems, quantum Monte Carlo, transient localization theory), in most cases approximations leading to analytical expressions are used. [1] These fall into the two categories of hopping and band-like transport via Boltzmann transport equation (BTE). The BTE approach, particularly suitable for orderly packed OSCs, is acknowledged for its precision when accounting for electronic structure details. However, to simplify equations, the effective mass approximation is commonly employed. [7]

In this study, we introduce a methodology for calculating and parameterizing the electron-phonon coupling (EPC) in organic semiconductors, and for using it to assess the OSC mobility. We validate the former by comparing it with experimental vibrational spectra, and the latter with experimental mobility values obtained from single crystals. Our investigation focuses on tetracene, a compound known for its various polymorphs. We observe differences between bulk polymorph 1 and thin-film polymorph, highlighting the need for comprehensive transport measurements on the latter. However, we recognize that the potential coexistence of these two phases, a phenomenon often detected in acenes, may pose a challenge in this task. [8,9]

## II. Computational method

## a. Electronic and Vibrational properties

On this ground, we follow the most effective state-of-the-art approach, [10–12] employing PBE pseudopotentials and the D3-BJ Grimme with Becke-Johnson damping functions for a posteriori VdW correction, [13] at any stage of a DFT calculation with VASP. [14,15] We start on the experimental unit cell parameters, optimize the k-points grid and then the energy cutoff for the wavefunctions, then relax the atomic positions keeping constant the unit cell parameters. Following relaxation, Phonopy packages [16,17] are used to compute and diagonalize the dynamical matrix using a  $2\times2\times2$  super-cell – a setup validated to ensure convergence in phonon frequency and 3D density of states (DOS) without any negative frequency, except for the acoustic branches in  $\Gamma$ , for which negative frequency around  $10^{-2}$  -  $10^{-3}$  THz may be obtained and are considered acceptable. Finally, the Raman spectrum is simulated by using the vasp\_raman.py code. [18] When comparing with experimental Raman spectra, the computed intensities have been adjusted by considering excitation wavelength and temperature dependence. [19] We consider this step mandatory to ascertain the suitability of the overall DFT scheme for the system under investigation.

# b. Electron-phonon coupling (EPC)

Following the previous procedure, we employ Phonopy to modulate the unit cell along the selected eigenmodes for  $\Gamma$  point and all the relevant high-symmetry q-points within the BZ, as given in the Bilbao crystallographic data center. [20,21] Thus, for each considered q point and  $\nu$  phonon branch, a unit cell distorted along the eigenmode vibrational coordinate is generated. Phonopy code automatically weights for the atomic mass in this process. In the tight-binding approximation the dispersion energy can be approximated along a 1D direction to  $\sim 2 t_W \cos(\mathbf{k} \cdot \mathbf{a})$ , and that leads to a bandwidth  $B_W$  related to the transfer integral  $t_W$  by the relation  $B_W = 4t_W$ . [22] As a result, the comprehensive bandwidth across the full 3D Brillouin Zone, and hence the corresponding transfer integral, can be obtained from a first principle DFT electronic structure calculation.

Under this conceptual framework, and taking into account the traditional approach to EPC [23,24] and the conventional definition of Deformation Potentials, [25,26] the EPC constant for each q-point and phonon branch  $\nu$  can be defined as:

$$D_{q,v}^{n,n} = \frac{\partial t_W^n}{\partial r_{q,v}} \tag{1}$$

$$D_{q,v}^{n,m} = \frac{\partial \Delta_s^{n,m}}{\partial r_{q,v}} \tag{2}$$

In eq.s (1)-(2), n and m are the band indexes,  $t_W^n$  is the bandwidth of the band of index n,  $\Delta_s^{n,m}$  is the Davydov splitting between the bands n and m, computed as the energy difference between the energy barycenters of the bands,  $r_{q,v}$  is the average displacements of all the atoms in the structure distorted along the eigenmode (q, v). Thus, Eq. (1) is related to *intra*-band processes, i.e. will be used when the carrier scattering involves initial and final states in the same band, while eq. (2) is related to *inter*-band processes.

Operatively, after a self-consistent DFT calculation for each (q, v) modulated/eigen-distorted structure, we perform a non-self-consistent calculation and save the obtained electronic structure in .bxsf format [27] with the c2x code. [28] Ad hoc routines were developed to extract the EPC parameters as in eq.s (1) and (2). Finally, since we will be considering states, and transitions, in the whole 3D electronic structure, a DOS-weighted average of the computed EPC was performed to extract band-index specific EPC parameters to be used throughout the whole BZ:

$$D_{n,m,\nu} = \frac{\sum_{q_{(\nu)}} D_{q,\nu}^{n,m^2} DOS_{q,\nu}}{\sum_{q_{|\nu|}} DOS_{q,\nu}}$$
(3).

The selection of the vibrational modes to be considered in this protocol relies on the phonon DOS specifications and is made considering altogether the modes which are bundled in the DOS. For tetracene, this encompasses the 16 modes of lowest frequency, with the additional eventual inclusion also of modes 17-20. This approach is exemplified in section III. The comprehensive EPC parametrized in eq. (3) are regarded as the proper deformation potentials for inelastic processes involving non-polar phonons in the mobility calculation, as detailed in the next sub-section.

### c. Mobility

Crystalline OSCs exhibit a well-defined crystal structure, which manifests in a distinctive vibrational fingerprint. Adopting a description based on the electronic dispersions in the BZ of the reciprocal lattice [29] the mobility  $\mu$  is evaluated from the conductivity  $\sigma$  as:

$$\mu_{ij(E_F,T)} = \frac{\sigma_{ij(E_F,T)}}{n \cdot q_0} \tag{4}$$

where i and j are the Cartesian components x, y, and z, of the mobility and conductivity tensors,  $E_F$  is the Fermi level, T the temperature, n the carrier density and  $q_0$  the electronic charge. The conductivity is computed in the context of the linearized BTE as:

$$\sigma_{ij(E_F,T)} = q_0^2 \int_E^{\square} \Xi_{ij}(E) \left( -\frac{\partial f_0}{\partial E} \right) dE$$
 (5)

The integrand of eq. 5 contains the Transport Distribution Function (TDF)  $\mathcal{Z}_{ij}$  and the energy derivative of the equilibrium Fermi-Dirac distribution  $f_0$ . The TDF is defined as:

$$\Xi_{ij}(E) = \frac{2}{(2\pi)^3} \sum_{n} \sum_{k_{n,E}} v_{i,k_{n,E}} v_{j,k_{n,E}} \tau_{i,k_{n,E}} g_{k_{n,E}}$$
(6)

In eq. 6 v is the band velocity,  $\tau$  the relaxation time, and g the electronic DOS. All these quantities are specific of each individual transport state  $k_{n,E}$ , where k is the wave-vector, n indicates the band index and E its energy. So, the sum runs over all the transport states identified by their momentum, belonging to all the bands, having a certain energy. The DOS  $g_{k_{n,E}}$  is defined as  $\frac{dA_{k_{n,E}}}{|\vec{v}_{k_{n,E}}|}$ , where  $dA_{k_{n,E}}$  represents the area of the surface element of the constant energy surface to which the  $k_{n,E}$  state belongs, associated to each specific  $k_{n,E}$  state. Therefore, the sum in eq. 6 is performed for each constant energy surface to compute the energy dependent TDF which will be then integrated as in eq. (5). In this work, the tetrahedron method has been employed to construct the constant energy surfaces and extract the related quantities. [30,31]

The relaxation time of the state  $k_{n,E}$  for the transport along the direction i, related to scattering with a phonon belonging to the branch  $\nu$ , is evaluated from the inelastic scattering with non-polar phonons as (we omit the index  $\nu$  for clarity): [25,26,31–33]

$$\frac{1}{\tau_{i,k_{n,E}}} = \frac{1}{(2\pi)^3} \sum_{\mathbf{k'}} \frac{\pi D_{n,n'}^2}{\rho \omega_0} \left( N_{\omega_0} + \frac{1}{2} \mp \frac{1}{2} \right) g_{\mathbf{k'}_{n',E'}} \left( 1 - \frac{v_{i,k'}_{n',E'}}{v_{i,k_{n,E}}} \right)$$
(7)

(7)

where D is the deformation potential related to the electron-phonon scattering between the initial band n and the final band n', which includes intra- and inter-band processes, evaluated from eq. (1) or (2), respectively.  $\rho$  is the mass density,  $\omega_{0,\nu} = \frac{\sum_{\omega_{\nu}} \omega_{\nu} \cdot DOS(\omega_{\nu})}{\sum_{\omega_{\nu}} DOS(\omega_{\nu})}$  is the dominant frequency for the branch  $\nu$  evaluated from a DOS-weighted average over the selected portion of the phonon spectrum,  $N_{\omega_0}$  represents the phonon Bose-Einstein statistical distribution,  $g_{k'_{n',E'}}$  is the DOS of the final state, belonging to the band n' and at energy E', which is either increased or decreased by  $\hbar\omega$  for absorption or emission processes, respectively, denoted by "–" and "+" signs. The term  $\left(1 - \frac{v_{i,k'_{n',E'}}}{v_{i,k_{n,E}}}\right)$  approximates the momentum relaxation time, [32–34] which is the relevant type of relaxation time for computing transport coefficients. [26] Note that this definition of relaxation time bears similarity to what appears in other works on OSCs. [35] The calculation of the mobility is performed using the ElecTra simulator. [29,36]

To perform the charge transport calculations, an additional non-self-consistent calculation on a finer mesh is needed. In this study, we adopted a  $30 \times 20 \times 15$  mesh with cutoff energy of 900 eV for the Polymorph 1 (P1) and  $28 \times 20 \times 12$  mesh with cutoff energy of 1000 eV for the thin film polymorph (PF), reaching the limit of the available node memory of the computing cluster. However, tests were run from a  $7 \times 5 \times 3$  grid onward and we found that a  $25 \times 15 \times 10$  grid provides convergence. Most important, the energy resolution used to construct the constant energy surfaces is set at 1 meV, meaning that each surface is calculated every 1 meV for each band, from the band edge up to  $\sim 0.4$  eV. Such fine resolution proves to be essential for the treatment of the flatter bands of the OSC compared to inorganic compounds. [31,37–39] Due to the large bandgap of tetracene, we perform unipolar calculations separately for electron mobility in the conduction band (CB) and hole mobility in the valence band (VB).

In addition to the main quantities described above, this work includes other quantities, computed when other processes needed to be accounted for. In the investigation of the role of punctual charged impurities, such as acceptors in the *p*-type case, the scattering with carriers was modeled as Ionized Impurity Scattering (IIS) within the Brooks-Herring framework:

$$\frac{1}{\tau^{IIS}_{i,k_{n,E}}} = \frac{1}{(2\pi)^3} \sum_{\mathbf{k'}} \frac{2\pi}{\hbar} \frac{Z^2 e^4}{k_S^2 \varepsilon_0^2} \frac{N_{imp}}{\left(|\mathbf{k} - \mathbf{k'}|^2 + \frac{1}{L_D^2}\right)^2} g_{\mathbf{k'}_{n',E'}} \left(1 - \frac{v_{i,k'}_{n',E'}}{v_{i,k_{n,E}}}\right)$$
(8)

where Z is the impurity charge,  $k_S$  the relative static permittivity, and  $L_D$  the screening length computed as

$$L_{\rm D} = \sqrt{\frac{k_{\rm S}\varepsilon_0}{q_0} \left(\frac{\partial n}{\partial E_{\rm F}}\right)^{-1}} \tag{9}.$$

We also discuss a diffusion mobility, defined from the Einstein relation as

$$\mu_{ij(E_F,T)}^D = \frac{q_0 D_{ij(E_F,T)}}{k_P T} \tag{10}$$

where the diffusion coefficient  $D_{i,j(E_F,T)}$  is computed starting from a DOS-weighted average of the transport state  $v_{i,k_{n.E}}v_{j,k_{n.E}}\tau_{i,k_{n.E}}$ , for each band, summing over all the bands:

$$D_{ij(E,E_F,T)} = \sum_{n} \frac{\sum_{k_{n,E}} v_{i,k_{n,E}} g_{k_{n,E}}}{\sum_{k_{n,E}} g_{k_{n,E}}}$$
(11)

An average over the carrier energy, also weighted by  $\frac{\partial f_0}{\partial E}$ , which approximates to  $f_0(1-f_0)$ , is performed to account for the states involved in transport:

$$D_{ij(E_F,T)} = \frac{\int D_{ij(E,E_F,T)} g_{(E)} \frac{\partial f_0}{\partial E} dE}{\int g_{(E)} \frac{\partial f_0}{\partial E} dE}$$
(12).

Finally, in the mean free path  $\lambda$  evaluation, a DOS-weighted average of the energy dependent mean free path is computed as:

$$\lambda_{i(E_{F},T)} = \frac{\sum_{E} \lambda_{i(E,E_{F},T)} g_{(E)}}{\sum_{E} g_{(E)}}$$
(13)

where *i* is the Cartesian coordinate,  $g_{(E)}$  the total electronic DOS, and each  $\lambda_{i(E,E_{\rm F},T)}$  term has the expression:

$$\lambda_{i(E,E_{F},T)} = \frac{\sum_{n,k_{n,E}} |v_{i(k,n,E)}\tau_{i(k,n,E,E_{F},T)}|g_{k_{n,E}}}{\sum_{n,k_{n,E}} g_{k_{n,E}}}$$
(14).

## III. Results and Discussion

# a. Description of the vibrational properties

The vibrational properties were computed for P1 [40] and PF [41,42] phases. The low temperature Polymorph II [43,44] was not considered as the atomic coordinates of this structure are, to the best of our knowledge, unknown. The phonon dispersions and the corresponding DOS are reported in Figure 1. It is important to note that the first 16 modes are bundled together throughout the BZ. Consequently, they have been treated collectively, with an effective frequency  $\omega_0$  and EPC assigned to them, as described in Section II. This feature is highlighted in Figure 1a, where the DOS for the two investigated polymorphs are reported. The dispersions along directions connecting high symmetry q-points are shown in Figure 1b and 1c for P1 and PF, respectively. Even in this case it is possible to observe how the 16 modes below 4.5 THz cross and intersect each other in the BZ. Additionally, in the thin film case, two upper modes slightly overlap with the lower 16; however, this minor overlap will be neglected in the following analysis. Since the lower 16 modes are bundled, we consider them as 16 scattering channels, following the common approach in semiconductors [26], and due to the dispersion through the BZ, we assign to each of them an effective phonon frequency  $\omega_0$ , computed as a DOS-weighted average of the phonon frequencies of that mode.

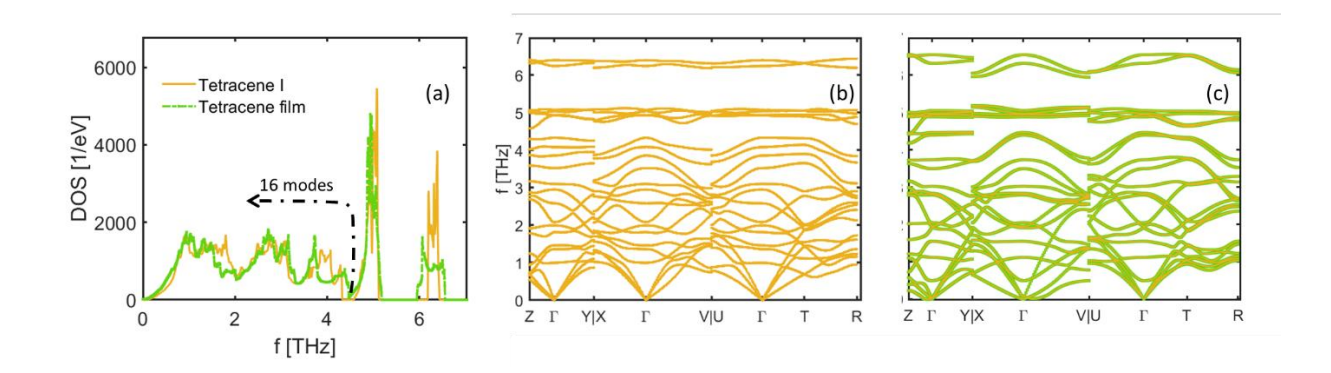


Figure 1: phonons DOS (a) and dispersions (b-c) for the P1 (orange) and the PF (green) polymorphs, respectively.

We further investigated the character of these modes by analyzing their Participation Ratio (PR) defined as: [45,46]

$$PR_{\boldsymbol{q},\nu} = \frac{1}{N_a} \frac{\left(\sum_a \frac{|e_{a,\boldsymbol{q},\nu}|^2}{m_a}\right)^2}{\sum_a \left(\frac{|e_{a,\boldsymbol{q},\nu}|^2}{m_a}\right)^2}$$
(15)

Where  $e_{a,q,v}$  is the phonon eigenvector for mode v in point q and atom a,  $m_a$  is the mass of atom a,  $N_a$  is the total number of atoms in the unit cell and the sums run over all the atoms in cell.

This parameter provides a normalized estimation of the fraction of atoms involved in the  $\nu$ -th vibrational mode. The spatial extension of such a group is linked to the localized or extended nature of that mode: for extended modes  $PR \sim 1$ , while localized modes have a smaller ratio, down to the limit  $PR = 1/N_a$  when the mode involves only a single atom.

The PR values for the first 16 modes are shown in Figure 2, for P1 and PF in (a) and (b), respectively. We can notice that at the zone boundaries, many modes display also a significant localized character. The extended character of the modes is more distributed over the BZ for the PF, with high PR values also at the zone boundaries, for some modes and q-points. When averaging the PR over this range, the thin-film phase shows a value nearly 3 % higher, 0.55 vs 0.53. Focusing on the nominal intermolecular modes, specifically the lowest 12 modes, the thin-film phase has a  $PR \sim 5$  % higher, 0.61 vs 0.58. A detailed description of the nature of rigid molecule modes in  $\Gamma$ can be obtained by projecting the eigenvectors along the rotational and translational coordinates in the molecular inertia axes system. In figure 2c,d the analysis of such decomposition of the lowest 16 modes in  $\Gamma$  is reported. DFT calculations can be validated by comparison with spectroscopic experiments, which probe frequencies at the  $\Gamma$  point. To accomplish this task, the off-resonant Raman activities were computed with the vasp Raman.py program. [18] This program uses VASP as back-end to compute the polarizability with the approach of the finite displacements, and returns the Raman activity of the selected modes. The results of the calculations in the low frequency range for P1 are compared with the experimental spectrum [43] in Figure 3a, with a zoom in the range of the experimental data in figure 3b. The spectra are drawn as Lorenzian bands with a fwhm of 1/3 of the mean distance between the frequencies, chosen to conform to the experimental features of P1. The positions of the peaks agree within a very few cm<sup>-1</sup>, less than 5, reported also in the S.I., thus confirming the validity of our description in terms of pseudopotentials and electronic structure. [11,12,47,48] The experimental relative intensities map satisfactorily on the simulated ones once the laser excitation frequency and the measurement temperature of the experiments are accounted for. [19] The fact that the experimental and computed peak positions agrees generally better than intensity ratios is not surprising, as it may stem on the unknown crystal orientation of the measured anisotropic specimen, [10,48] which determines which components of the polarizability matrix, and thus the band intensities, were actually probed in the experiment. Additionally, figures 3c and 3d present the Raman spectrum of the polymorph, not yet reported experimentally, highlighting clear differences that can guide future experimental spectroscopic studies. [12,47,48]

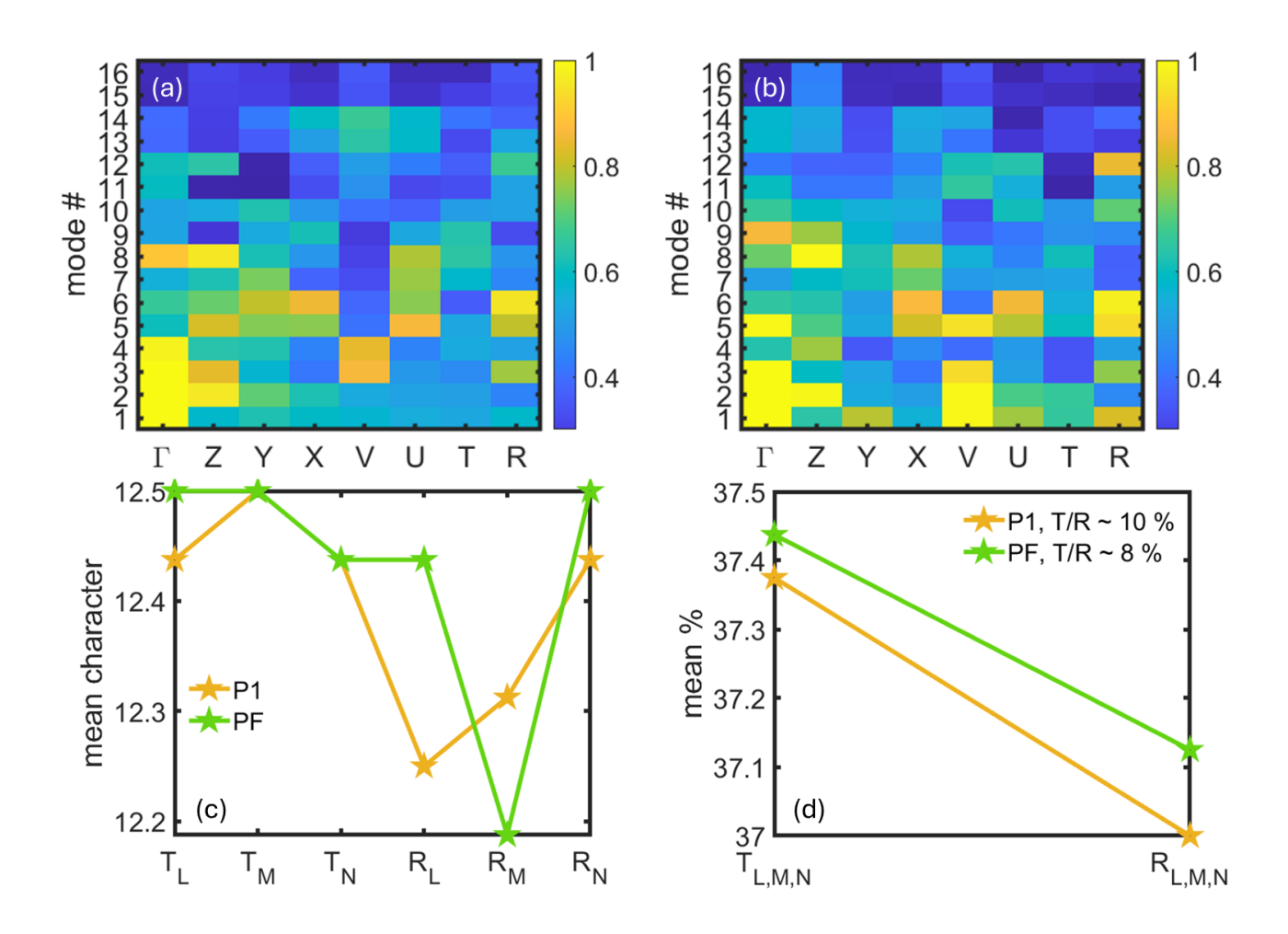


Figure 2: PR values at different BZ high symmetry q-points, for the lower 16 modes, (a) P1, (b) PF. We observe a slightly higher extended character in the PF modes, especially in the lower modes and far off  $\Gamma$ , whereas in the P1 the high extended character is mostly limited to BZ center. (c) Mode decomposition in  $\Gamma$  along translational (T) and rotational (R) eigenvectors, averaged for all the modes. (d) The mode average L, M, and N, components of T and R have been summed, it appears that the PF modes have an average larger extended character, and a larger R character in comparison of the T one.

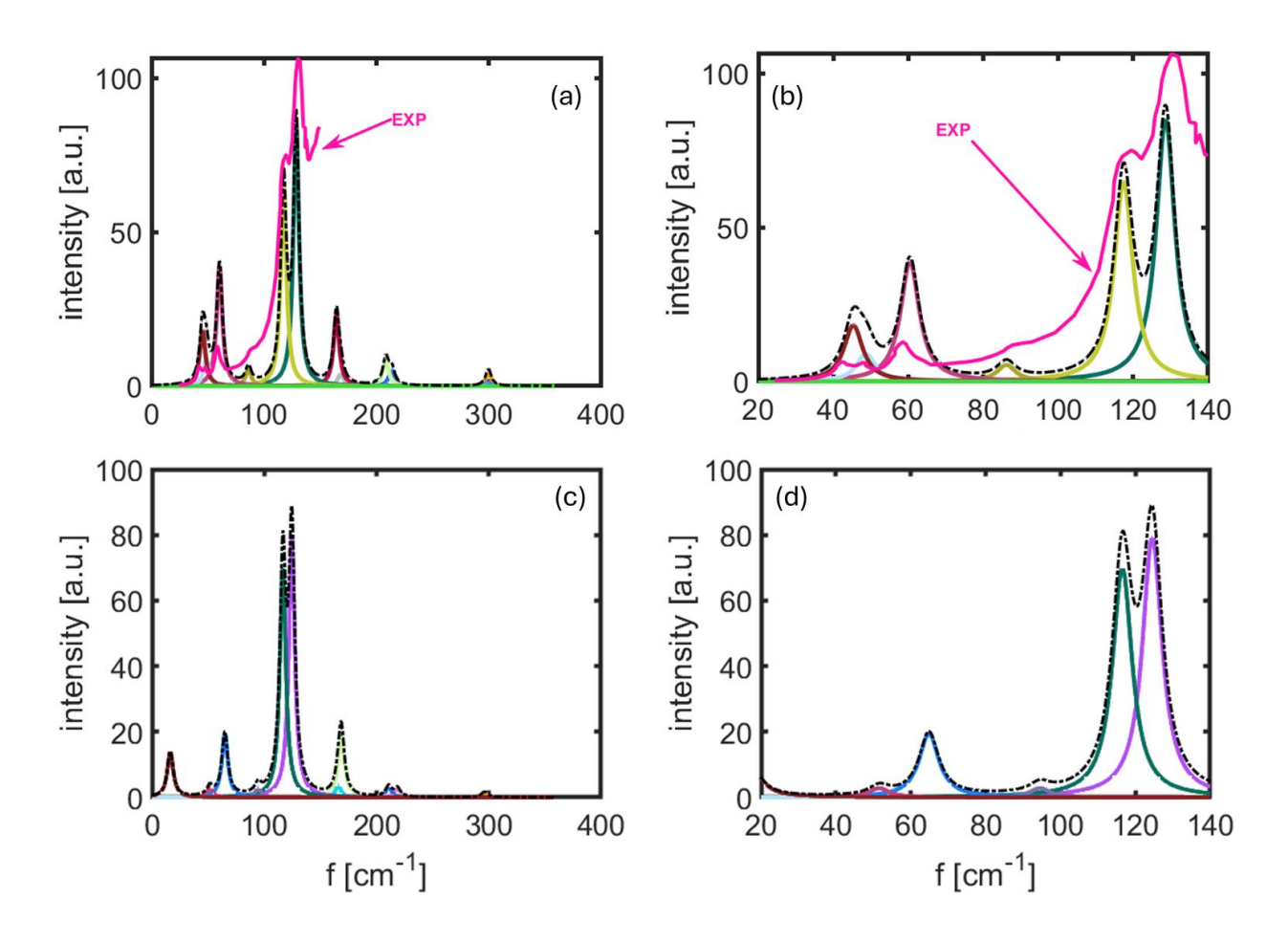


Figure 3: (a) and (b), validation of the DFT protocol that compute the electronic and vibrational structure via comparison between computed and experimental Raman spectra of the P1, the experimental data, in magenta line, have been obtained from ref. [43]. The experimental intensities have been transformed into Raman activities by accounting for measurement temperature and laser frequency. (c) and (d), the Raman spectra of the PF are shown, on the same frequency ranges.

### b. EPC parameters

In this section, we present the EPCs evaluation according to eq.s (1)-(3). They have been computed with Phonopy for unit cells with atoms displaced along each eigenmode, employing an input amplitude of 0.1, which results in an average displacement of the order of  $10^{-4}$ Å. The test on the convergence of such values with respect to the displacement is detailed in the Supporting Information. Figures 4 and 5 show the EPCs computed for P1 and PF, respectively, from the different bands and the Davydov splitting. The terms CB and VB refer to conduction band and valence band, respectively, with  $1^{st}$  and  $2^{nd}$  indicating the order from the edge, with the former having the lower minimum.

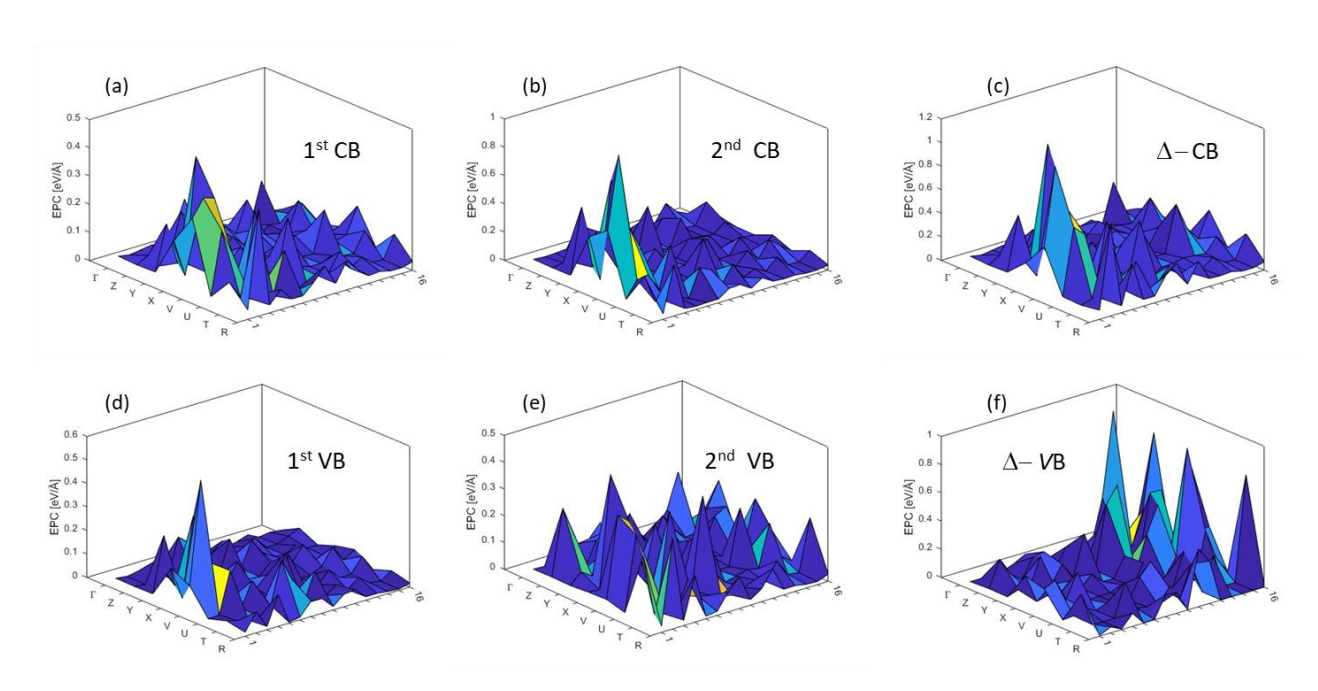


Figure 4: EPC values in eV/Å for tetracene bulk, comprising the lowest 16 modes at 8 high symmetry **q**-points in the BZ, as indicated. (a) and (b), EPC computed with eq. (1) for the two CBs, (c) EPC computed from the Davydov splitting as in eq. (2). (d)-(f), same as (a)-(c) for the VBs.

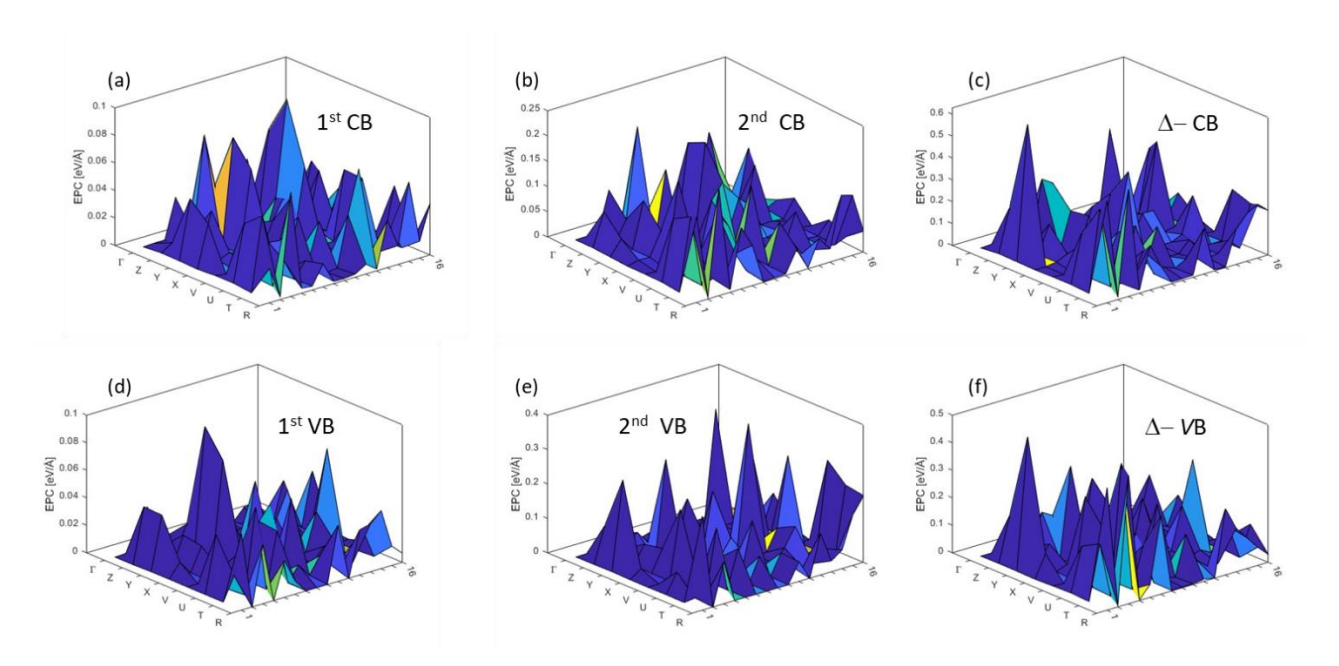


Figure 5: EPC values in eV/Å for tetracene PF, comprising the lowest 16 modes at 8 high symmetry **q**-points in the BZ, as indicated. (a) and (b), EPC computed with eq. (1) for the two CBs, (c) EPC computed from the Davydov splitting as in eq. (2). (d)-(f), same as (a)-(c) for the VBs.

From Figures 4 and 5 we can deduce that certain modes, at specific **q**-points of the BZ, i.e. with a given momentum, lead to very strong EPC, whereas at other **q**-points the EPC strength is much lower. Since our task is to describe the scattering across the entire BZ, in every direction, we must average

them. [38] This holds not only for each individual mode, but also for all of them together, given their strong bundled feature. Thus, the values in Figures 3 and 4 must be weighted for the DOS and averaged as from eq. (3). Mode and q-points specific EPC values are listed in the Supporting Information.

The EPC values obtained though this procedure are reported in the S.I., whereas in table I we provide the sum of the EPC of each mode as a one-number rough indication of the EPC strength, labelled EPC\*, in units of eV/Å. The same table also lists the bandwidths (BWs), which are related to the transfer integrals between translationally equivalent molecules ( $\alpha$  or  $\beta$ ) in different unit cells. [49] Thus, a larger BW indicates a stronger interaction between translationally equivalent molecules in different unit cells of the crystal. This might lead to higher insensitivity to the modulation carried by the vibrational modes.

|           | VB1   | VB2   | inter-band | CB1   | CB2   | inter-band |
|-----------|-------|-------|------------|-------|-------|------------|
| P1 – EPC* | 1.27  | 1.69  | 2.80       | 1.54  | 2.35  | 3.39       |
| P1 - BW   | 0.191 | 0.189 | 0.013      | 0.268 | 0.351 | 0.060      |
| PF – EPC* | 0.32  | 1.36  | 1.88       | 0.41  | 1.0   | 2.17       |
| PF - BW   | 0.525 | 0.342 | 0.252      | 0.30  | 0.467 | 0.198      |

Table I: EPC, in eV/Å, and bandwidth BW, in eV, for the CB and VB of the two polymorphs. The column "inter-band" contains, for the EPC, the inter-band scattering term, for the BW, the amount of the overlap between the two bands. It is possible to observe that the PF has much broader bandwidths.

The electron 3D DOS and band velocity, computed in the reciprocal unit cell on the mesh used for the subsequent transport calculations and over the adopted energy range, are depicted in Figure 6. The two VBs and two CBs lie quite separated in P1, when the DOS drops and then raises again. In contrast, these bands are more bundled in PF, leading to higher total band velocity in this polymorph.

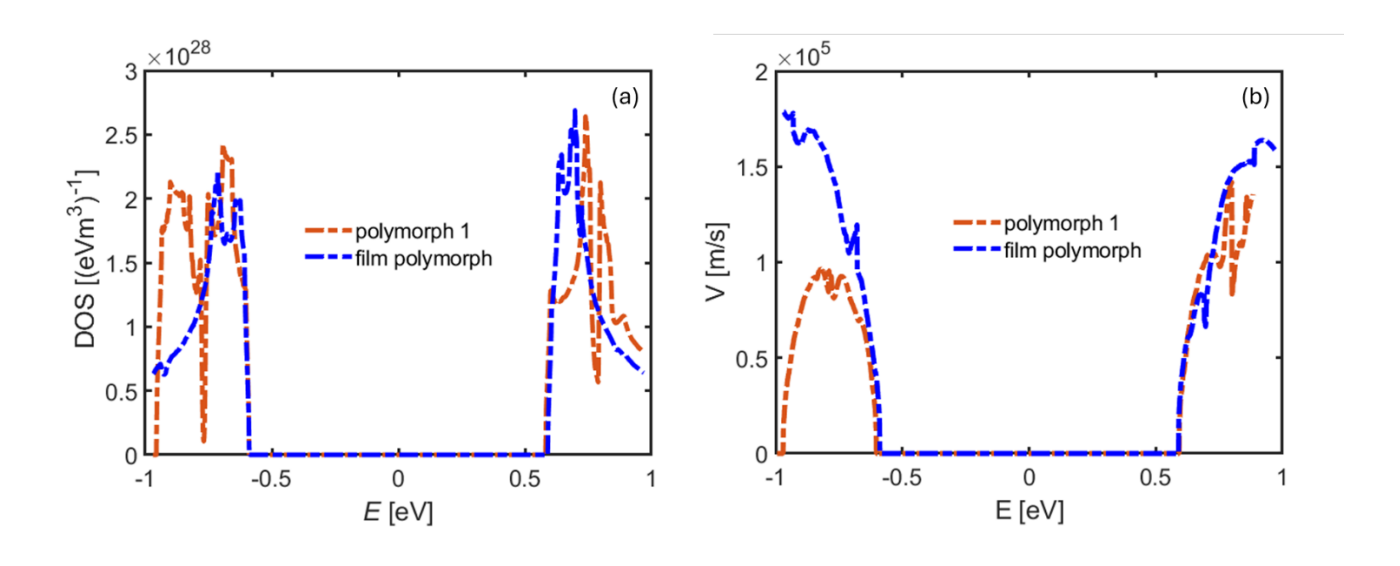


Figure 6: (a) density-of states (DOS) and (b) band velocity, in S.I. units, for the two tetracene polymorphs investigated. Two CB bands and two VBs band can be distinguished in the P1 where the DOS falls down and raises again, so that bands have little energy overlap; in the PF the overlaps are more significant. The computed bandgaps are narrower than the experimental ones, as common in DFT calculations, [50–52] however this does not affect the computed unipolar mobility.

## c. Mobility

In this section, the mobility is computed using the approach provided in section II.c. The mobility tensor derived using equations (4)-(7) is in Cartesian coordinates.

First, we project the electric field  $\overrightarrow{\mathcal{E}_i}$  along the crystallographic axes. This is achieved by inverting the lattice vector matrix, expressed in the POSCAR VASP file:

$$\overrightarrow{\mathcal{E}_{l}} = \boldsymbol{a} * \text{inv}(A) \tag{16}$$

where a is the intended direction in the internal coordinates and A is the lattice vector matrix. This allows us to express the electric fields along the internal cell axes,  $\overrightarrow{\mathcal{E}_a}, \overrightarrow{\mathcal{E}_b}$ , and  $\overrightarrow{\mathcal{E}_c}$  in Cartesian coordinates. Next, from the conductivity tensor  $\overline{\sigma}$ , given by eq. 5, we compute a current density as:

$$\vec{J_l} = \overline{\bar{\sigma}} \vec{\mathcal{E}_l} \tag{17}.$$

Thus, we obtain a component of the conductivity tensor in internal coordinates:

$$\sigma_i = \frac{|\vec{J_i}|}{|\vec{\mathcal{E}_i}|}$$
 (18)

and the related mobility:

$$\mu_i = {}^{\sigma_i}/n \cdot q_0 \tag{19}.$$

Using this approach, we can link the computed mobility tensor in Cartesian coordinates to the mobility measurable along specific crystal directions.

We first aim at validating our approach by comparing computed and experimental data. Considering that the reported experimental values vary widely, mostly due to extrinsic phenomena, mobilities measured in single crystals should be regarded as the relevant reference. [53,54] The experimental minimum mobility  $\mu_{\perp ab}$ , measured perpendicular to the ab plane in tetracene single-crystal OFETs [54]is plotted alongside the corresponding computed mobility in Figure 7. In particular, panel (a) compares the experimental mobility (in black) to the *p*-type mobility (in yellow) computed for a Fermi level placed at approximately  $\frac{1}{4}$  of the bandgap. We observe that the computed mobility is of the correct order of magnitude, though somewhat larger.

Additional insights are gained from the analysis of the power law exponent in  $\mu \sim T^n$ . By fitting all the experimental data together, black line in Figure 7a, an exponent of -2.56 is computed. When splitting the analysis to distinguish between high and low temperature regimes, the low temperature one (red dotted line) gives an exponent of -4.50, while the low temperature (green dotted line) gives an exponent of -1.77. The computed BTE mobility (orange stars and orange dash-dot lines) returns an exponent of -1.69, which is very close to the experimental mobility at low T, whereas for the diffusion mobility, this exponent is much lower. This convinced us that the description based on the DFT electronic structure, which accurately reproduces the experimental Raman spectra, can be regarded as a solid basis also for transport simulations in crystalline OSCs. Thus, our findings suggest that the common BTE mobility is more suitable than the diffusion mobility to describe the OSCs. Finally, we performed a mobility calculation that included, in the same foot of the lowest 16 modes, the next 4 modes between 4.5 and 5.5 THz, which form a bundled group in the DOS right above 4.5 THz. However, no significant differences were detected in the mobility values despite this additional scattering process involving a larger ensemble of modes. This suggests that our approach, that considers the lower bundled modes up to the chosen threshold, together with the method for computing and parametrize EPC, appears suitable to describe the mobility of the OSC under investigation.

We stress that the experimental single crystal mobility appears to be limited by the traps at the metal/OSC contact interface and that shallow traps in this region are likely to strongly decrease the mobility by more than 70 %, making difficult to have an unambiguous experimental reference for the mobility. [54] Based on this, we included punctual defects in the model. These defects act as electron acceptors and behave like p-dopants. We also assume that the carrier density is completely due to these impurities, which consistently downshift the Fermi level towards the band edge. From the perspective of carrier scattering, the defects are treated in the framework of the IIS described in section II.c. Their charge was set either equal to one or ½, at densities comparable to those estimated for OSC crystals. [55,56] The choice of a ½ charge should simulate a situation where the charge of the ionized acceptor is effectively spread over more molecules, resembling an extended charged defect. The results for two densities of ionized defects are plotted in magenta in Figure 7 (b). We can see that the calculated mobility values fall within the experimental range, although with a reduced slope in the T dependence. This demonstrates that mobilities can be brought within the interval of the experimental values by considering defects, although, undoubtedly, a better description of these would be necessary. This is even more true for the case of FET mobility, where the determinant role of scattering at the boundary between differently oriented regions has been observed by in-operando

kelvin-force measurements. [57] This scattering is likely responsible of a measured tetracene mobility [58,59] which is lower than the one estimated for bulk single crystals. [54]

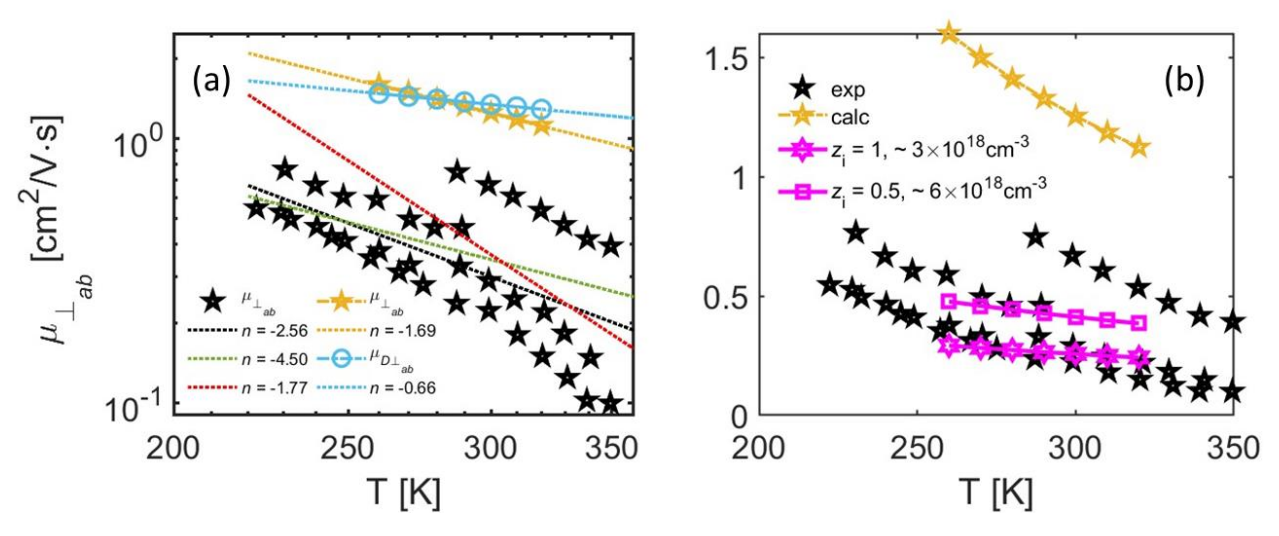


Figure 7: (a) comparison between experimental mobility values measured perpendicular to the ab plane, [54] and the computed values,  $\mu_{\perp ab}$ . The diffusion mobility computed from eq.s (10)-(12) is also shown, indicated as  $\mu_{\perp ab}^D$ . The corresponding fits are displayed, as explained in the main text. (b) mobilities computed with the addition of punctual ionized defects, considered as electron acceptors, at two different concentrations and ionized charges. The fractional charge aims at mimicking extended charged defects. By including these, the match between the experimental and computed mobilities improves, but at the cost of a change in the T dependence. However, this suggests that the overestimation of the computed mobility is likely due to the neglect of extrinsic charged defects.

Eq. (16) allows us to express the electric field in the internal coordinates, enabling the analysis of the mobility anisotropy within the crystal planes. This is demonstrated for the hole and the electron transport in P1 in Figure 8 (a) and (b), respectively. For each plane, the lines are plotted by using over  $10^6$  random directions on the plane. A uniaxial anisotropy appears, that means that a direction of higher mobility is present, which is nearly parallel to the *b* axis. This direction lies in the *ab* plane, which is generally the contact plane for OFETs, and is consistent with what observed in other OSCs like pentacene or rubrene. [60,61] Moreover, we obtain an anisotropy ratio of the mobility in the *ab* plane of 3, in good agreement with the experimental findings, which is around 2. [62,63] Additionally, the approach outlined in eq.s (16)-(19) can be used to obtain random 3D orientations and compute an average mobility over more than  $10^6$  random orientations. We plot this mobility  $\mu_r$  in Figure 8 (c). Such a random mobility can be regarded as a reference mobility in a specimen with crystallites in several orientations, even though the carrier scattering at the boundaries between the crystallites is anyway neglected. The same analysis for the PF is shown in Figure 9.

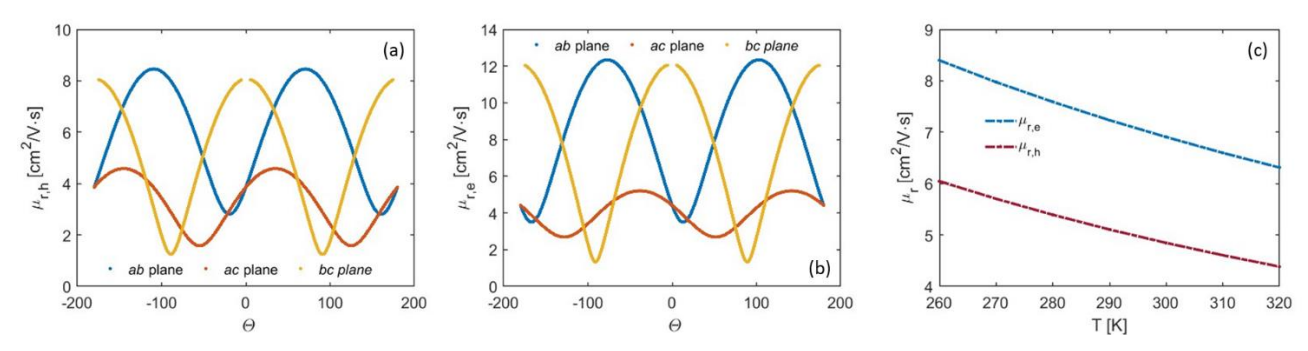


Figure 8: (a) anisotropic hole mobility in the crystal planes, as indicated;  $\Theta$  is the angle, in deg, in respect of a cell axis. (b) anisotropic electron mobility in the crystal planes, as indicated. The average in-plane mobility is  $\mu_{ab} \sim 6.1$  (8.5) cm<sup>2</sup>/Vs,  $\mu_{ac} \sim 3.1$  (4.3) cm<sup>2</sup>/Vs,  $\mu_{bc} \sim 5.7$  (8.5) cm<sup>2</sup>/Vs for holes (electrons). The in-plane anisotropy ratios are 3.0 (3.5), 2.9 (1.9), 6.5 (9.1), for the *ab*, *ac*, and *bc* planes, respectively, for holes (electrons). (c) average mobility computed for  $2 \cdot 10^6$  random orientations of the electric field.

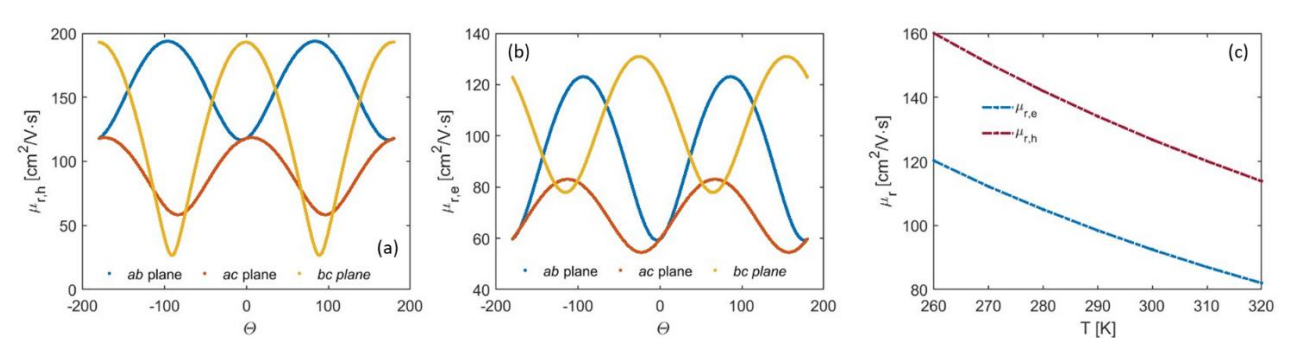


Figure 9: (a) anisotropic hole mobility in the crystal planes, as indicated;  $\Theta$  is the angle, in degrees, with respect to the cell axis. (b) anisotropic electron mobility in the crystal planes, as indicated. The average in-plane mobility is  $\mu_{ab} \sim 157.9$  (94.3) cm<sup>2</sup>/Vs,  $\mu_{ac} \sim 91.2$  (68.9) cm<sup>2</sup>/Vs,  $\mu_{bc} \sim 130.7$  (104.4) cm<sup>2</sup>/Vs for holes (electrons). The in-plane anisotropy ratios are 1.7 (2.1), 2.0 (1.5), 7.3 (1.7), for the *ab*, *ac*, and *bc* planes, respectively, for holes (electrons). (c) average mobility computed for  $2 \cdot 10^6$  random orientations of the electric field.

We observe that the PF presents a much higher mobility. The idea that some polymorphs of acenes exhibit higher mobility is not new, to the extent that it has been suggested that the wide variability in mobility observed in pentacene OFETs can be attributed to the presence of different crystal forms, [64] and coexistence of structures has been detected. [9,65] So, the disorder is increased by the coexistence of polymorphs, with detrimental impact on the mobility. Thin films phases, also known as surface induced structures, [66] are particularly important in applications such as OFETs,

as the OSC conducting channel lie at the interface with the dielectric layer. [67] In fact, pentacene thin-film structure has been reported to exhibit a higher mobility than the bulk. [68] The TF mobility here calculated is for a single crystal, i.e. for a 3D, highly pure system which, in fact, is actually experimentally unattainable, as this phase exists only within a few nm thickness before coexist with, or being replaced by, the bulk polymorph. [8] However, this result suggests that, similar to pentacene, the thin-film phase exhibits improved charge transport characteristics.

Our goal now is to address the reasons behind the higher mobility of the PF. This can be due to the higher carrier band velocity, Figure 6, but mostly to the lower EPC strength, up to  $\sim 4 \times$  lower in the topmost VB and lowest CB – we recall that the scattering rate has a quadratic dependence on the EPC. We further challenge this task by addressing the average random mobility, the bandwidth, an average electronic structure quantity, the EPC, the interaction between the electronic structure and the vibrational modes. The bandwidth of the two CBs and the two VBs for each polymorph is reported in Figure 10 (a), where the x-axis is the average energy of the band. It is obvious that the PF has wider, more disperse, bands, which correspond to the larger velocity in Figure 6. The positive relationship between more disperse bands and mobility is demonstrated in Figure 10 (b), where the random mobility computed after eq.s (16)-(19) is plotted in respect of the CB and VB bandwidth of the two polymorphs, here we considered the topmost VB and the lowest CB, denoted with '0' subscript, as they are the most involved in the charge transport. To gain additional insight into this qualitative consideration, we investigate the relationship between the random mobility at 300 K and the ratio between the bandwidth, which favors the mobility, and the EPC strength, which drops the mobility, is reported in Figure 10 (c). As we did in table I, to lump the EPC of all the phonon modes in just one number, we consider the sum of them. Here, a straightforward trend appears, which tells the two key ingredients to have high mobility OSC: large bandwidth and weak EPC.

Thus, the core task becomes how to achieve weak EPC, and, in our case, what gives such lower EPC in PF. We believe that wider electronic bands, signature of more stable interactions, can be a relevant hint. Also, the question whether a larger BW signals a greater insensitivity of the transfer integral to the phonon modes, is worth deeper investigation.

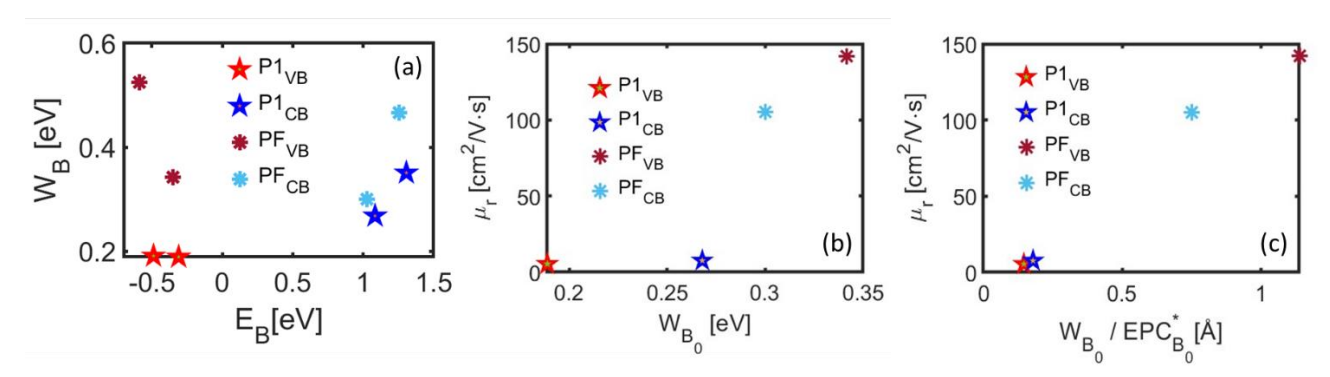


Figure 10: (a) total band width versus band energy, evaluated as the mean of the band eigenvalues, for the two valence bands (VB), bright red, and two conductions bands(CB), bright blue, of P1, and, with dark red and light blue, the same for PF. (b) dependence of the random mobility at 300 K, Eq.s (16)-(19), versus the average bandwidth of the two VBs or CBs for the two polymorphs. A clear monotonic dependence appears. (c) values of the average EPC strengths for the same bands, where it is possible to observe that the PF bands have lower EPC. (d) dependence on the random mobility at 300 K with respect of the ratio between the bandwidth and the EPC, for the bands at the edge, i.e. the topmost VB and the lowest CB, which are the bands more involved in the transport. A clear dependence appears, signaling the relevant parameters for mobility in OSC.

### IV. Conclusions

A method has been developed that combines DFT-level calculations and semiclassical transport simulations to compute the electron-phonon coupling in the model organic semiconductor tetracene. The coupling has been estimated across the Brillouin zone for different phonon modes, and from these calculations, the charge mobility has been evaluated. The validity of the electronic structure and phonon calculations has been demonstrated by computing the low frequency Raman spectrum and comparing it with experimental results. Based on this achievement, the suitability of the overall method has been confirmed through a comparison of computed and experimental single-crystal hole mobility. An overestimated mobility of approximately twice the experimental value is obtained; however, including point ionized defects adjusts the mobility to fall within the experimental range at the cost, however, of a worse agreement in its overall temperature dependence. This suggests that the development of a proper treatment for likely extended ionized defects is necessary to achieve accurate modeling of real specimens. Furthermore, the ratio between the bandwidth and the EPC is identified as a key parameter for ranking the mobility of OSCs.

We demonstrate that our approach is suitable for first-principles calculations of mobility in crystalline OSCs. Our work establishes a solid foundation for understanding how polymorphism impacts electronic properties and devises a simulation approach to link solid-state packing and charge transport.

## Acknowledgement

We are thankful to prof. Alberto Girlando for fruitful discussions, to Dr. Andra Giunchi for supporting in the computational protocol for the Raman spectra. We acknowledge the CINECA award under the ISCRA initiative, for the availability of high performance computing resources and support. We acknowledge funding from the European Union—Next-Generation EU via the Italian call PRIN 2022, project code 2022XZ2ZM8, "POLYPHON". T.S. thanks the Programma per Giovani Ricercatori "Rita Levi Montalcini" year 2020 (grant PGR20QN52R) of the Italian Ministry of University and Research (MUR) for the financial support. We acknowledge funding for the VASP license from the company M.M.B. s.r.l., Faenza (RA) Italy.

#### References

- [1] Ö. H. Omar, M. del Cueto, T. Nematiaram, and A. Troisi, J. Mater. Chem. C 9, 13557 (2021).
- [2] J. M. Ha, S. H. Hur, A. Pathak, J.-E. Jeong, and H. Y. Woo, NPG Asia Mater 13, 1 (2021).
- [3] J. Ma, Y. Li, N. S. Grundish, J. B. Goodenough, Y. Chen, L. Guo, Z. Peng, X. Qi, F. Yang, L. Qie, C.-A. Wang, B. Huang, Z. Huang, L. Chen, D. Su, G. Wang, X. Peng, Z. Chen, J. Yang, S. He, X. Zhang, H. Yu, C. Fu, M. Jiang, W. Deng, C.-F. Sun, Q. Pan, Y. Tang, X. Li, X. Ji, F. Wan, Z. Niu, F. Lian, C. Wang, G. G. Wallace, M. Fan, Q. Meng, S. Xin, Y.-G. Guo, and L.-J. Wan, J. Phys. D: Appl. Phys. 54, 183001 (2021).
- [4] S. Fratini, M. Nikolka, A. Salleo, G. Schweicher, and H. Sirringhaus, Nat. Mater. 19, 491 (2020).
- [5] O. G. Kharlanov, D. R. Maslennikov, E. V. Feldman, G. G. Abashev, O. V. Borshchev, S. A. Ponomarenko, M. V. Vener, D. Yu. Paraschuk, and A. Yu. Sosorev, Advanced Electronic Materials 7, 2100579 (2021).
- [6] G. Schweicher, G. D'Avino, M. T. Ruggiero, D. J. Harkin, K. Broch, D. Venkateshvaran, G. Liu, A. Richard, C. Ruzié, J. Armstrong, A. R. Kennedy, K. Shankland, K. Takimiya, Y. H. Geerts, J. A. Zeitler, S. Fratini, and H. Sirringhaus, Advanced Materials 31, 1902407 (2019).
- [7] I. Yavuz, Phys. Chem. Chem. Phys. 19, 25819 (2017).
- [8] R. K. Nahm and J. R. Engstrom, The Journal of Chemical Physics **146**, 052815 (2016).
- [9] A. Brillante, I. Bilotti, R. G. Della Valle, E. Venuti, A. Girlando, M. Masino, F. Liscio, S. Milita, C. Albonetti, P. D'angelo, A. Shehu, and F. Biscarini, Phys. Rev. B **85**, 195308 (2012).
- [10] A. Giunchi, L. Pandolfi, R. G. Della Valle, T. Salzillo, E. Venuti, and A. Girlando, Crystal Growth & Design 23, 6765 (2023).
- [11] T. Kamencek, S. Wieser, H. Kojima, N. Bedoya-Martínez, J. P. Dürholt, R. Schmid, and E. Zojer, J. Chem. Theory Comput. **16**, 2716 (2020).
- [12] T. Salzillo, S. d'Agostino, A. Rivalta, A. Giunchi, A. Brillante, R. G. Della Valle, N. Bedoya-Martínez, E. Zojer, F. Grepioni, and E. Venuti, J. Phys. Chem. C **122**, 18422 (2018).

- [13] N. Bedoya-Martínez, A. Giunchi, T. Salzillo, E. Venuti, R. G. Della Valle, and E. Zojer, J. Chem. Theory Comput. **14**, 4380 (2018).
- [14] G. Kresse and J. Furthmüller, Phys. Rev. B 54, 11169 (1996).
- [15] G. Kresse and J. Furthmüller, Computational Materials Science 6, 15 (1996).
- [16] A. Togo, J. Phys. Soc. Jpn. 92, 012001 (2023).
- [17] A. Togo, L. Chaput, T. Tadano, and I. Tanaka, J. Phys.: Condens. Matter 35, 353001 (2023).
- [18] (2024).
- [19] D. Michalska and R. Wysokiński, Chemical Physics Letters 403, 211 (2005).
- [20] M. I. Aroyo, D. Orobengoa, G. de la Flor, E. S. Tasci, J. M. Perez-Mato, and H. Wondratschek, Acta Crystallographica Section A **70**, 126 (2014).
- [21] (n.d.).
- [22] C. Winkler, F. Mayer, and E. Zojer, Advanced Theory and Simulations 2, 1800204 (2019).
- [23] A. Girlando, L. Grisanti, M. Masino, I. Bilotti, A. Brillante, R. G. Della Valle, and E. Venuti, Phys. Rev. B 82, 035208 (2010).
- [24] M. Masino, T. Salzillo, A. Brillante, R. G. Della Valle, E. Venuti, and A. Girlando, Advanced Electronic Materials **6**, 2000208 (2020).
- [25] Electron Transport in Compound Semiconductors | SpringerLink (n.d.).
- [26] M. Lundstrom, *Fundamentals of Carrier Transport*, 2nd ed. (Cambridge University Press, Cambridge, 2000).
- [27] A. Kokalj, Journal of Molecular Graphics and Modelling 17, 176 (1999).
- [28] M. J. Rutter, Computer Physics Communications 225, 174 (2018).
- [29] P. Graziosi, Z. Li, and N. Neophytou, Computer Physics Communications 287, 108670 (2023).
- [30] G. Lehmann and M. Taut, Physica Status Solidi (b) **54**, 469 (1972).
- [31] P. Graziosi, C. Kumarasinghe, and N. Neophytou, Journal of Applied Physics 126, 155701 (2019).
- [32] N. Neophytou and H. Kosina, Phys. Rev. B 83, 245305 (2011).
- [33] N. Neophytou and H. Kosina, Phys. Rev. B 84, 085313 (2011).
- [34] M. V. Fischetti and S. E. Laux, Journal of Applied Physics 80, 2234 (1996).
- [35] S. Fratini and S. Ciuchi, Phys. Rev. Res. 2, 013001 (2020).
- [36] P. Graziosi, (2024).
- [37] P. Graziosi, C. Kumarasinghe, and N. Neophytou, ACS Appl. Energy Mater. 3, 5913 (2020).
- [38] Z. Li, P. Graziosi, and N. Neophytou, Phys. Rev. B **104**, 195201 (2021).
- [39] Z. Li, P. Graziosi, and N. Neophytou, Npj Comput Mater 10, 1 (2024).
- [40] D. Holmes, S. Kumaraswamy, A. J. Matzger, and K. P. C. Vollhardt, Chemistry A European Journal 5, 3399 (1999).
- [41] L. Pithan, D. Nabok, C. Cocchi, P. Beyer, G. Duva, J. Simbrunner, J. Rawle, C. Nicklin, P. Schäfer, C. Draxl, F. Schreiber, and S. Kowarik, The Journal of Chemical Physics **149**, 144701 (2018).
- [42] Pithan, Linus, Nabok, Dmitrii, Cocchi, Caterina, Beyer, Paul, Duva, Giuliano, Simbrunner, Joseph, Rawle, Jonathan, Nicklin, Chris, Schäfer, Peter, Draxl, Claudia, Schreiber, Frank, and Kowarik, Stefan, https://doi.org/10.5517/CCDC.CSD.CC1ZXHLZ.
- [43] E. Venuti, R. G. Della Valle, L. Farina, A. Brillante, M. Masino, and A. Girlando, Phys. Rev. B **70**, 104106 (2004).
- [44] R. G. Della Valle, E. Venuti, A. Brillante, and A. Girlando, J. Phys. Chem. A 110, 10858 (2006).
- [45] A. Antidormi, X. Cartoixà, and L. Colombo, Phys. Rev. Mater. 2, 056001 (2018).
- [46] T. Kamencek, N. Bedoya-Martínez, and E. Zojer, Phys. Rev. Mater. 3, 116003 (2019).
- [47] N. Bedoya-Martínez, B. Schrode, A. O. F. Jones, T. Salzillo, C. Ruzié, N. Demitri, Y. H. Geerts, E. Venuti, R. G. Della Valle, E. Zojer, and R. Resel, J. Phys. Chem. Lett. **8**, 3690 (2017).
- [48] T. Salzillo, A. Giunchi, M. Masino, N. Bedoya-Martínez, R. G. Della Valle, A. Brillante, A. Girlando, and E. Venuti, Crystal Growth & Design **18**, 4869 (2018).
- [49] Y. C. Cheng, R. J. Silbey, D. A. da Silva Filho, J. P. Calbert, J. Cornil, and J. L. Brédas, The Journal of Chemical Physics **118**, 3764 (2003).
- [50] J. C. Sorli, P. Friederich, B. Sanchez-Lengeling, N. C. Davy, G. O. N. Ndjawa, H. L. Smith, X. Lin, S. A. Lopez, M. L. Ball, A. Kahn, A. Aspuru-Guzik, and Y.-L. Loo, J. Mater. Chem. C 9, 1310 (2021).

- [51] J. P. Perdew, W. Yang, K. Burke, Z. Yang, E. K. U. Gross, M. Scheffler, G. E. Scuseria, T. M. Henderson, I. Y. Zhang, A. Ruzsinszky, H. Peng, J. Sun, E. Trushin, and A. Görling, Proceedings of the National Academy of Sciences **114**, 2801 (2017).
- [52] Á. Morales-García, R. Valero, and F. Illas, J. Phys. Chem. C **121**, 18862 (2017).
- [53] M. E. Gershenson, V. Podzorov, and A. F. Morpurgo, Rev. Mod. Phys. 78, 973 (2006).
- [54] R. W. I. de Boer, M. Jochemsen, T. M. Klapwijk, A. F. Morpurgo, J. Niemax, A. K. Tripathi, and J. Pflaum, Journal of Applied Physics **95**, 1196 (2004).
- [55] H. T. Yi, Y. N. Gartstein, and V. Podzorov, Sci Rep 6, 23650 (2016).
- [56] D. D. T. Mastrogiovanni, J. Mayer, A. S. Wan, A. Vishnyakov, A. V. Neimark, V. Podzorov, L. C. Feldman, and E. Garfunkel, Sci Rep 4, 4753 (2014).
- [57] P. Annibale, C. Albonetti, P. Stoliar, and F. Biscarini, J. Phys. Chem. A 111, 12854 (2007).
- [58] V. Y. Butko, X. Chi, and A. P. Ramirez, Solid State Communications 128, 431 (2003).
- [59] H. Morisaki, T. Koretsune, C. Hotta, J. Takeya, T. Kimura, and Y. Wakabayashi, Nat Commun **5**, 5400 (2014).
- [60] J. Y. Lee, S. Roth, and Y. W. Park, Applied Physics Letters 88, 252106 (2006).
- [61] F. Ortmann, F. Bechstedt, and K. Hannewald, Physica Status Solidi (b) 248, 511 (2011).
- [62] E. G. Bittle, A. J. Biacchi, L. A. Fredin, A. A. Herzing, T. C. Allison, A. R. Hight Walker, and D. J. Gundlach, Commun Phys **2**, 1 (2019).
- [63] Y. Xia, V. Kalihari, C. D. Frisbie, N. K. Oh, and J. A. Rogers, Applied Physics Letters 90, 162106 (2007).
- [64] A. Landi, A. Troisi, and A. Peluso, J. Mater. Chem. C 7, 9665 (2019).
- [65] C. Westermeier, A. Cernescu, S. Amarie, C. Liewald, F. Keilmann, and B. Nickel, Nat Commun **5**, 4101 (2014).
- [66] A. O. F. Jones, B. Chattopadhyay, Y. H. Geerts, and R. Resel, Advanced Functional Materials **26**, 2233 (2016).
- [67] C. d. Dimitrakopoulos and P. r. l. Malenfant, Advanced Materials 14, 99 (2002).
- [68] C. D. Dimitrakopoulos, A. R. Brown, and A. Pomp, Journal of Applied Physics 80, 2501 (1996).